

# Magnetic Remote Activation of Shape Recovery in Nanocomposites Based on Tung Oil and Styrene

Cintia Meiorin, Daniel G. Actis, Fabiano E. Montoro, Oscar Moscoso Londoño, Mirta I. Aranguren, Diego Muraca,\* Pedro Mendoza Zélis,\* Marcelo Knobel, and Mirna A. Mosiewicki\*

The activation of unconstrained shape recovery in bio-based polymeric nanocomposites is successfully achieved using magnetic nanoparticle heating. The materials investigated in this work present several distinct physical and chemical characteristics worth pointing out: they can be deformed and the original shape can be recovered by remotely heating the samples above their switching temperature, which is determined by their glass transition temperatures. Also, their chemical composition is largely based on biomass (the polymeric matrix contains more than 50 wt.% of raw tung oil). Magnetic heating performance is strongly affected by both the physical properties and the concentration of the nanoparticles loaded into the matrix. The concentration of nanoparticles is associated with the formation of agglomerates or clusters, which determines the dipolar interactions among the nanoparticles. The particles used in this work are able to absorb enough energy from an alternating magnetic field to heat the matrix and initiate the shape recovery. Although the sample with the highest content of magnetic solute (10 wt.%) presents the highest degree of agglomeration, it is also the sample with the best remote activation of shape recovery, according to the temperature reached under magnetothermal measurements and the time of actuation.

of the natural raw materials is very important to consider the chemical groups that can participate directly in polymerization reactions or that can be modified to prepare polymeric precursors of industrial interest. In the last decade, there has been an increase in the number of publications, reviews, books, and scientific conferences on this topic.<sup>[2,4,8,9]</sup> At the same time, there has been an increasing participation of the public and industrial sectors all around the world in the promotion and financing of research and development of applications in this field, focusing on the search of alternatives to solve economic and environmental issues.

Vegetable oils are renewable raw materials used in the production of a wide variety of commercial products, many of them related with non-edible industrial applications, such as coatings, inks, plasticizers, lubricants, and paints.<sup>[8,9]</sup> Under specific synthesis conditions, thermosetting and thermoplastic polymers derived from vegetable oils can exhibit characteristics com-

parable to those petroleum-based commercial products.<sup>[10,11]</sup> Frequently, biomass-based materials are only partially bio-based in order to better tailor the final required properties for a given application. For example, some formulations are prepared by mixing synthetic and renewable resins. Renewable polymer

## 1. Introduction

The most widely used bio-based polymers are based on renewable resources that include vegetable oils, polysaccharides (mainly cellulose and starch), and proteins.<sup>[1–7]</sup> In the selection


Dr. C. Meiorin, Prof. M. I. Aranguren, Prof. M. A. Mosiewicki  
Instituto de Investigaciones en Ciencia y Tecnología de Materiales (INTEMA)  
Universidad Nacional de Mar del Plata–Consejo Nacional de Investigaciones Científicas y Técnicas (CONICET)  
Av. J. B. Justo 4302, 7600 Mar del Plata, Argentina  
E-mail: mirna@fi.mdp.edu.ar

Dr. C. Meiorin, Prof. D. Muraca, Prof. M. Knobel  
Instituto de Física Gleb Wataghin (IFGW)  
Universidade Estadual de Campinas – UNICAMP  
Rua Sérgio Buarque de Holanda, 777 - Cidade Universitária Zeferino Vaz Barão Geraldo 13083-859 - Campinas Sao Paulo, Brazil  
E-mail: diego.muraca@gmail.com

Dr. D. G. Actis, Prof. P. Mendoza Zélis  
Instituto de Física La Plata (IFLP-CONICET)  
Universidad Nacional de La Plata  
Diagonal 113, Casco Urbano, 1900 La Plata, Argentina  
E-mail: pmendoza@fisica.unlp.edu.ar

F. E. Montoro  
Laboratorio Nacional de Nanotecnología (LNNano/CNPEM)  
Rua Giuseppe Maximo Scolfaro 10000  
13083-100 Campinas, São Paulo, Brazil

Prof. O. Moscoso Londoño  
Facultad de Ingeniería  
Universidad Autónoma de Manizales Antigua Estación del Ferrocarril  
170001 Manizales, Caldas, Colombia

 The ORCID identification number(s) for the author(s) of this article can be found under <https://doi.org/10.1002/pssa.201800311>.

DOI: 10.1002/pssa.201800311

precursors can be obtained by different chemical modifications of selected vegetable oils.<sup>[12,13]</sup> In particular, tung oil is extracted from the seeds of the tung tree and composed mainly of  $\alpha$ -elaeostearic acid.<sup>[14,15]</sup> This vegetable oil is a highly unsaturated with conjugated double bonds, which are responsible for its excellent drying properties that are widely appreciated in the paint and varnish industry.

Publications referred to reactions of raw vegetable oils or mixtures of them with a reactive vinyl comonomer (e.g., styrene) indicate that, in general, free radical copolymerization is not a viable path for the preparation of materials with good dimensional stability because the carbon–carbon unsaturations in triglycerides are not reactive enough.<sup>[16]</sup> However, in the presence of a cationic initiator, highly unsaturated vegetable oils (e.g., tung oil, modified linseed oil) and derived reactive monomers cannot only lead to materials having excellent mechanical performance, but also to ones that can exhibit shape memory behavior. This depends mainly on the formulation of the initial reaction mixture and the polymerization conditions.<sup>[11]</sup>

Smart polymers with shape memory behavior are materials that can be deformed and retain their “temporary-induced” shape, until a self-response is triggered by an external stimulus so that the original or “permanent” shape is recovered. The shape memory response can be activated by inducing changes in temperature, humidity, light intensity, stress, magnetic or electric-applied fields, which lead to changes in the molecular conformation of the polymer. Probably, the most frequently used triggering factor in these types of materials is temperature. In this case, the polymer undergoes an important behavioral change at a particular temperature (for simplicity, called switching temperature), which can be related to the glass transition temperature,  $T_g$ , or to the melting temperature,  $T_m$ , depending on the polymer structure (thermoset or thermoplastic polymers, respectively). The polymer considered in this work has the structure of a crosslinked network. By increasing the temperature above its  $T_g$ , its elastic modulus is dramatically reduced and the network can be mechanically deformed. The achieved shape can be temporarily fixed by reducing the temperature while maintaining the sample under the mechanical load. When a temperature lower than  $T_g$  is reached, the mechanical load can be removed and the temporary shape remains fixed. To recover the original shape (stored because of the crosslinked structure of the network), the material is heated again above its  $T_g$ .

Shape memory materials are applied in the fields of medicine,<sup>[17]</sup> aerospace industry,<sup>[18]</sup> coatings,<sup>[19]</sup> toys,<sup>[20]</sup> optic materials,<sup>[21]</sup> textile industry,<sup>[22]</sup> and electronics,<sup>[23]</sup> among others. They can also present special interesting additional attributes as self-healing ability, for example.<sup>[24]</sup> It is worth noting that each specific application presents particular requirements that may include the analysis of toxicity, biocompatibility, biodegradability, as well as mechanical, thermal, and chemical responses. Different authors have investigated how to tune the elastic modulus that could be achieved by the incorporation of rigid nanoparticles.<sup>[25–28]</sup> Even more, new interesting properties could be obtained when the nanoparticles also incorporate functional properties to the composite, for example, magnetic ones. This is especially attractive because the magnetic

properties of these nanoparticles can be used to remotely activate the shape self-recovery of smart materials. When magnetic nanostructures are subjected to alternating magnetic fields, an electromagnetic energy conversion into heat occurs and consequently, the surrounding medium where they are embedded increases its temperature. Thus, it is possible to heat the composite, which will self-recover the original shape if the switching temperature is reached during the process. The efficiency that the magnetic nanoparticles have to transform energy absorbed from an alternating magnetic field into heat is usually characterized through the specific absorption rate (SAR) parameter.<sup>[29–31]</sup> This remote activation has been utilized most commonly in the heating of segmented linear polyurethanes, for which the switching temperature is the melting one of the soft segments.<sup>[32–36]</sup> Few researchers have also considered the incorporation of magnetite nanoparticles into polymer networks, to remotely activate shape memory behavior. In those cases, the chosen matrices were not based on biomass.<sup>[37,38]</sup>

The aim of this work was to investigate the effect of the incorporation of magnetic nanoparticles into a polymeric matrix with high bio-based content and shape memory behavior. Specifically, the structural, magnetic, and induced-heating properties were analyzed, mainly focusing on the magnetically induced shape recovery of the nanocomposites. For this purpose, a thermoset with low glass transition temperature was synthesized through the cationic polymerization of raw tung oil and styrene. On the other hand, magnetic iron oxide nanoparticles with a mean size of 10 nm were prepared by an alkaline co-precipitation method and further coated with oleic acid in order to hydrophobize their surfaces and make them compatible with the lipid-based polymer.

The structural characterization of the nanocomposites and particles embedded into them (shape, size, and presence of agglomerates) was performed by transmission electron microscopy and small-angle X-ray scattering (SAXS). Magnetic studies were carried out by zero field cooling-field cooling (ZFC-FC) and magnetization versus field measurements, obtaining parameters of the nanoparticles such as the blocking and irreversible temperatures, magnetization at high fields and coercive values. These properties were correlated with SAR values and remote shape recovery process.

## 2. Experimental Section

### 2.1. Materials

Tung oil was a commercial product supplied by Cooperativa Agrícola Limitada de Picada Libertad, Argentina. It is composed mainly of the triester formed with glycerol and  $\alpha$ -elaeostearic acid (84 wt.%). Styrene (St) and tetrahydrofuran (THF) were purchased from Cicarelli Laboratory, Argentina. Boron trifluoride diethyl etherate ( $\text{BF}_3 \cdot \text{OEt}_2$ ) with 46–51%  $\text{BF}_3$  was obtained from Sigma–Aldrich and used as the initiator of the cationic reaction.

For the magnetic nanoparticles preparation, the following reagents (Sigma–Aldrich) were used as received: ferric chloride hexahydrate ( $\text{FeCl}_3 \cdot 6\text{H}_2\text{O}$ ), ferrous chloride tetrahydrate ( $\text{FeCl}_2 \cdot 4\text{H}_2\text{O}$ ), ammonium hydroxide (28–30%  $\text{NH}_3$ ), and oleic acid; n-heptane was used as solvent (P.A. grade).

## 2.2. Methods and Techniques

### 2.2.1. Magnetic Nanoparticles (MNPs) Preparation

Magnetic iron oxides nanoparticles were prepared by a co-precipitation method from an aqueous  $\text{Fe}^{3+}/\text{Fe}^{2+}$  solution using excess of concentrated ammonium hydroxide (solution 30%  $\text{NH}_3$ ). Specifically, 0.09 mol of  $\text{FeCl}_3 \cdot 6\text{H}_2\text{O}$  and 0.06 mol of  $\text{FeCl}_2 \cdot 4\text{H}_2\text{O}$  were dissolved in 50 mL of distilled water and heated at 70 °C. After that, 40 mL of  $\text{NH}_4\text{OH}$  were added and the formation of a black precipitate was immediately observed.<sup>[39]</sup>

The obtained nanoparticles were subsequently coated by adding 0.02 mol of oleic acid and heating the suspension to 80 °C for 30 min under stirring. The obtained oleic acid-coated MNPs were washed with distilled water and separated by centrifugation several times until neutral pH was obtained. Finally, they were dispersed in n-heptane to form a stable ferrofluid and stored until its use. The obtained nanoparticles presented a mean size of 9.8 nm and their characterization was previously reported.<sup>[39]</sup>

### 2.2.2. Preparation of Bio-Based Compounds and Magnetic Nanocomposites

From the result of previous studies,<sup>[39–41]</sup> a formulation of tung oil/styrene (weight ratio of 50/50) was selected as the polymeric matrix with shape memory behavior. The monomers mixture was stirred and this step was followed by the addition of the modified initiator prepared by mixing THF (5 wt.% with respect to the reactive mixture) with boron trifluoride diethyl etherate (3 wt.% with respect to the reactive mixture). Oleic acid-coated MNPs (1.5, 3, 5, 7, or 10 wt.%) were incorporated to the original mixture. The code names for the resulting nanocomposites were 1.5MNP, 3MNP, 5MNP, 7MNP, and 10MNP, respectively. Then, the suspensions were subjected to ultrasonication to obtain a good dispersion of the nanoparticles and finally, poured into glass plates of  $13 \times 18 \text{ mm}^2$  separated by a rubber cord of 1 mm of thickness and kept closed with metal clamps. The reactants were heated, first at 60 °C for 12 h and then, at 100 °C for 24 h.<sup>[39]</sup> After curing, the samples were conditioned at room temperature (RT), inside a desiccator containing silica gel to maintain a dry atmosphere.

### 2.2.3. Scanning Transmission Electron Microscopy (STEM)

All images were acquired using a “Dual Beam FEI Helios Nanolab 660” microscope. The samples were fractured and covered with carbon by electron beam in a “LEICA MED 020” equipment. The images were obtained with acceleration voltage of 20 kV, beam current of 100 pA, and working distance (WD) of 4 mm. Secondary electron images were obtained with the In-Lens TLD detector (Through Lens Detector) and the back-scattered electron images were acquired with a CBS detector (Concentric Rings Backscattered Detector) using the two innermost segments of the detector (segments A and B) to improve the contrast of materials.

To prepare thin samples for STEM, the 10MNP composite was embedded in Eponate 12 resin, cured for 16 h at 60 °C and cut using an ultramicrotome “RMC Boeckeler Power Tome XL.” Thin samples with thickness between 10 and 100 nm were obtained and deposited on a 400 Mesh copper grid. STEM images of these sections were obtained with a concentric ring STEM detector (FEI third generation detector) using acceleration voltage of 30 kV, working distance of 4 mm, and currents between 1.6 and 13 pA.

### 2.2.4. Small-Angle X-ray Scattering (SAXS)

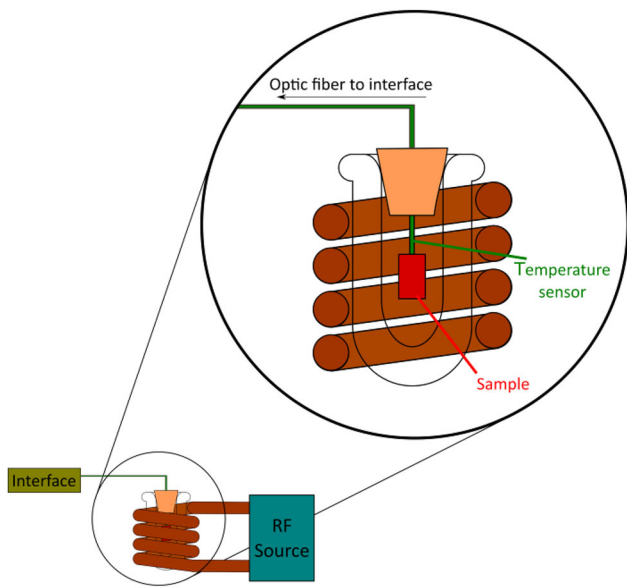
SAXS experiments were performed at the SAXS2 beamline at the Brazilian Synchrotron Light Laboratory (LNLS), Centro Nacional de Pesquisa em Energia e Materiais (CNPEM), Campinas, Brazil. The scattering intensity was measured as function of momentum transfer vector  $q$  ( $q = 4\pi \sin\theta/\lambda$ ), in the range from 0.08 to  $2.0 \text{ nm}^{-1}$ , being  $\theta$  the scattering angle and the wavelength,  $\lambda = 1.822 \text{ \AA}$ . All SAXS experiments were conducted under controlled environmental conditions (20 °C and  $45 \pm 5\%$  relative humidity). Data treatment was performed using SASfit package.<sup>[41]</sup>

### 2.2.5. Static Magnetic Properties

Magnetic properties of the nanocomposites were studied using a SQUID magnetometer (Quantum Design, MPMS XL7). The magnetization is reported as the ratio of magnetic moment per mass of sample. The magnetic field dependence of magnetization was measured with field up to  $1600 \text{ kA m}^{-1}$  (20 kOe) at various temperatures. Magnetization versus temperature curves were obtained in zero field cooled (ZFC) and field cooled (FC) modes. In the ZFC mode, the sample was cooled under a zero magnetic field. Then, a static magnetic field of  $4 \text{ kA m}^{-1}$  was applied and the magnetization was recorded as the temperature was increased up to 300 K. In the FC mode, the sample was cooled in the presence of a magnetic field of  $4 \text{ kA m}^{-1}$  and the magnetization was measured during warming under the same field.

### 2.2.6. SAR

The sample's specific absorption rate, a quantifier of its capacity to transfer energy from the radio frequency field (RF) to its medium via heat dissipation, was determined by means of magnetocalorimetric measurements in magnetic nanoparticle heating experiments: the sample was exposed to an alternating magnetic field ( $48 \text{ kA m}^{-1}$  and 260 kHz) while its temperature was recorded (**Scheme 1**). The measurements were performed with the sample placed in a Dewar flask fixed at the center of a coil. The circuit was powered by a source-resonator set Hüttinger TIG 2.5/300. The sample temperature was measured by an optic fiber sensor (Neoptix T1) immersed in the center of the material and connected to an interface (Neoptix Reflex). The sample was initially at room temperature and the experiment was interrupted when the temperature of the sample reached 340 K.



**Scheme 1.** Schematics of the configuration used to generate the alternating magnetic field at the sample's position, and to record its temperature versus time.

### 3. Results and Discussion

#### 3.1. Morphological Analysis

Electron microscopy (STEM) was used to analyze the morphology of the nanocomposites. **Figure 1a** shows an image of the 10MNP sample obtained from backscattered electrons while **Figure 1b** shows an image obtained by the superposition of backscattered electrons and secondary electrons. This last image allows observing simultaneously the matrix morphology and the particles distributed inside, offering an improved two dimensional rendering of the obtained three dimensional structures. From the analysis of the images obtained from different parts of the sample, it was concluded that different types of structures can be found in the material. Specifically, it can be said that a bimodal cluster size distribution was detected. The smallest clusters (SCs) show a near spherical shape, with a mean diameter of  $314 \pm 40$  nm. The inset of **Figure 1a** shows the size distribution of these SCs with the corresponding lognormal fit used to determine the average size of the clusters. On the other

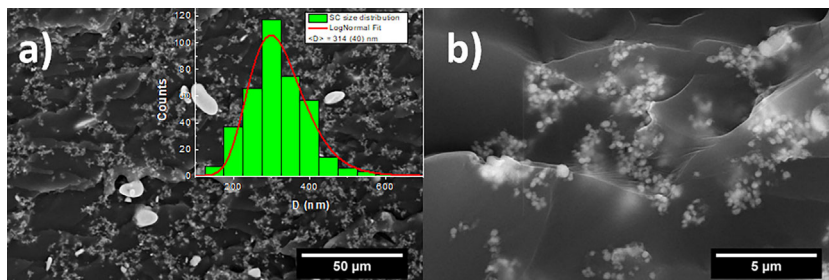


**Figure 1.** a, b) Micrographs of sample 10MNP obtained by STEM at different magnifications. Right corner inset of (a): size distribution of SCs.

hand, the biggest clusters (BCs) have an ellipsoidal shape, with minimum length axes between 900 and 2500 nm and maximum length axes between 1500 and 8000 nm, respectively. The occurrence of these BCs was 1–500 with respect to that of the smaller ones. Due to the small quantity of BCs, it was difficult to estimate with precision their size distribution, nevertheless the maximum axis length was 1.4–3 times higher than the minimum axis length.

In addition, the SCs form bigger agglomerates with a well-defined fractal structures. In **Figure 1a** and **b**, it can be seen that these clusters formed by the smaller ones seem to percolate the whole volume of the film. This was observed for all the samples with nanoparticles concentration equal or higher than 3 wt.%. For the sample 1.5MNP, these fractal structures are isolated from each other forming separated islands (see **Figure S1**, Supporting Information). STEM images of the lamellas prepared by ultramicrotomy allowed obtaining better images of the internal structures of the smaller clusters (**Figure S2**, Supporting Information). **Figure 2a** and **b** show a better resolution of these clusters obtained by STEM-BF (bright field) of a 100 nm slice. From high-angle annular dark-field and due to high scattering angles of the electrons produced by the Fe atoms we could infer the presence of the magnetic nanoparticles on the clusters (**Figure 2c**). Even more, it was possible to observe the individual nanoparticles (of near 10 nm) on each cluster (**Figure 2d**) using STEM-BF images of a 10 nm slice. Images from both observation modes (**Figure 2** and **Figure S3**) confirmed a non-compact agglomeration of the nanoparticles, i.e., a very thin coating that avoids the direct contact of the nanoparticles is still present on the material.

To confirm the composition on the different clusters, the chemical elemental analysis of them was recorded by means of energy dispersive spectroscopy (EDS). **Figure 3** shows the EDS analyses of the SCs and the BCs, respectively. From these, the presence of Fe (K1-edge) and O (K1-edge) was confirmed in each type of cluster.

#### 3.2. SAXS Analysis

The SAXS technique was used to investigate the structural organization of the magnetic nanoparticles within the matrices. The scattering intensity profiles for every investigated sample, presented in a log–log plot, are displayed in **Figure S4**, Supporting Information. All of the scattering patterns seem to follow similar trends, which are characteristic of systems composed by polydisperse nanoparticles and their aggregates.<sup>[42–45]</sup> That is, at the low- $q$  region, the scattering intensity follows a particular power law, instead of the Guinier behavior for individual and non-interacting nanoparticles, indicating the formation of aggregates of MNPs within the matrices. For high- $q$  values, all of the patterns follow a power law of  $I(q) \sim q^{-4}$  (Porod's law), expected due to the smooth and sharp interfaces among the MNPs and the host matrices.

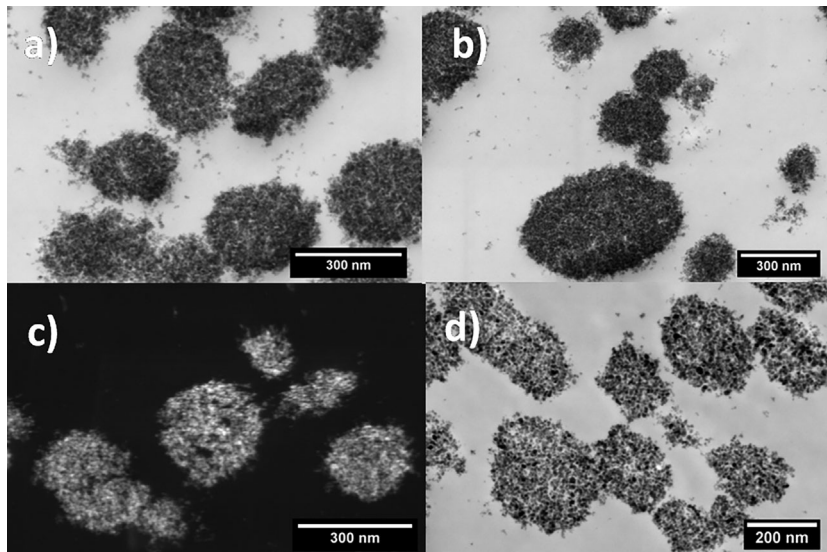


**Figure 2.** STEM images of the lamellas prepared by ultramicrotomy for the sample 10MNP.

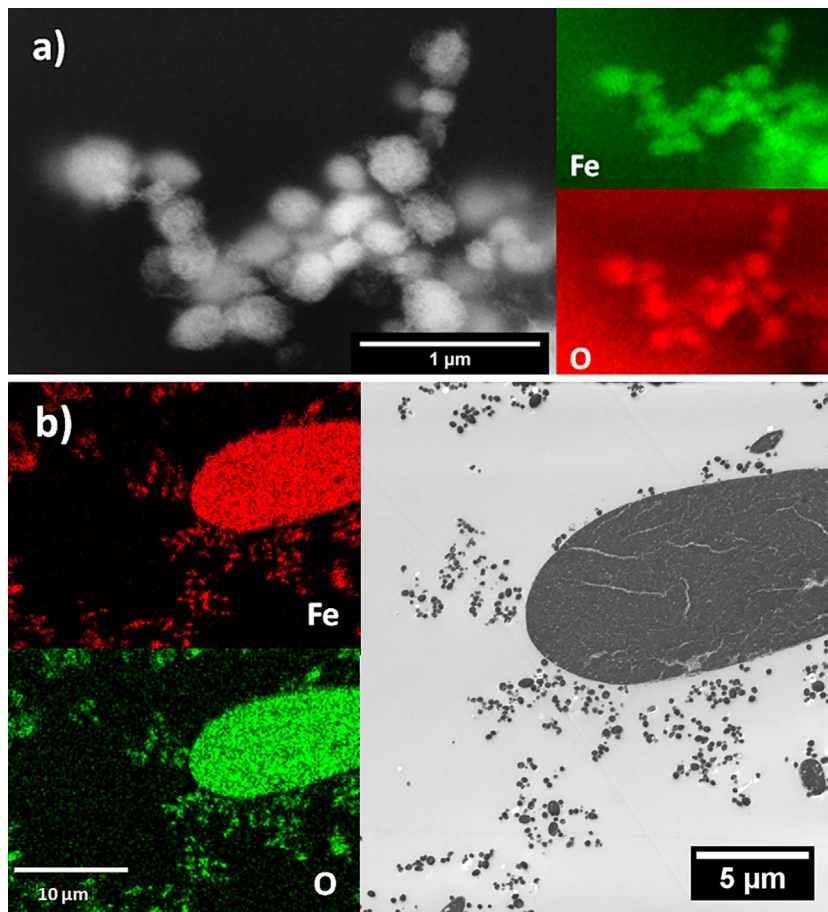


**Figure 3.** EDS analyses of the smaller clusters, a) SCs and b) bigger clusters, BCs.

The observed differences in the power law behavior at low- $q$  region (Guinier zone) are due to different scattering interferences between the neighboring iron oxide nanoparticles in every sample, indicating that the arrangements of the MNPs inside the matrices are directly related to the nanoparticle concentration. As it can be noted (Figure S4, Supporting Information), a power law of  $I(q < 0.1 \text{ nm}^{-1}) \sim q^{-2.7}$  was found for the matrix loaded with 10 wt.% of magnetic nanoparticles, with the exponent progressively decreasing until reaching a scattering intensity dependence of  $\approx q^{-1.8}$  in the samples with lower amount of magnetic nanoparticles. This behavior can be explained as the result of the formation of more compact and possibly larger aggregates as the nanoparticle concentration increases, as it was observed in previous works.<sup>[42,45]</sup>

Based on the microscopy and SAXS results presented, it is possible to infer that samples with content of MNPs equal or larger than 3 wt.% can be analyzed taking into account a bimodal distribution of clusters with fractal structures (big and small clusters, BCs and SCs, respectively), where every cluster is formed by primary nanoparticles. Notice that the measured  $q$ -range covers those scattering objects matching the size of the small clusters observed by STEM. In that sense, the experimental SAXS data were analyzed using the exponential/power-law model postulated by Beaucage, which combines the Porod and Guinier regimes to describe the scattering intensity produced by systems containing multiple levels with related structural features.<sup>[46]</sup> Here, we propose two interrelated structural levels: aggregates and individual primary nanoparticles. Then, the expression used to describe scattering intensity of this kind of systems is given by

$$\begin{aligned}
 I(q) \cong & G \exp\left(\frac{-q^2 Rg^2}{3}\right) \\
 & + B \exp\left(\frac{-q^2 Rs^2}{3}\right) \left(\frac{\text{erf}(qRg/\sqrt{6})}{q}\right)^{Df} \\
 & + Gs \exp\left(\frac{-q^2 Rs^2}{3}\right) \\
 & + Bs \left(\frac{\text{erf}(qRg/\sqrt{6})}{q}\right)^P
 \end{aligned} \quad (1)$$

being  $G$  and  $B$  the Guinier and Porod pre-factors of the smaller cluster (SCs);  $G_s$  and  $B_s$  are the corresponding pre-factors of the primary nanoparticles,  $Rg$  is the radius of

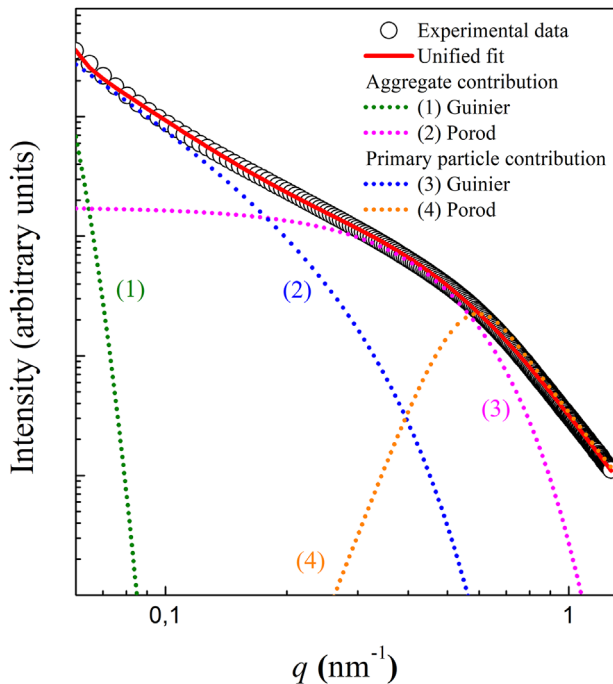


**Figure 4.** Experimental data (empty circles) and fitting of Equation (1) with SASfit package (solid line) and the different contributions of Beaucage model for the sample 10MNP: (1) Guinier aggregates, (2) Porod aggregates, (3) Guinier individual particles, (4) Porod individual particles.

gyration of the SCs structures,  $R_s$  the radius of the primary nanoparticles,  $D_f$  is the fractal dimension and  $P$  is the Porod exponent and  $erf$  is the error function. Thus, the first term describes the structure of those clusters labeled as SCs and the second one carries the information of the fractal structure,<sup>[41]</sup> while the last ones contain the structural information related to the primary nanoparticles.

As it can be observed in **Figure 4**, the Beaucage approach successfully describes the scattering intensity from a set of MNPs, which are arranged forming clusters of larger size. For the fitting procedure, the nanoparticle radius was restricted to values between 4 and 4.9 nm according to the transmission electron microscopy (TEM) information reported in a previous work.<sup>[39]</sup> Then, by following the Beaucage expression, parameters as  $R_g$ ,  $D_f$ , and  $P$  were estimated, from which a progressive increase in  $D_f$  and  $R_g$  (and hence in the size of the SCs,  $\xi$ ) was observed (see **Table 1**), while the values found for the Porod

**Table 1.** SAXS parameters obtained using Equation (1).

Sample	$R_g$ [nm]	$D_f$	$P$	$\xi$ [nm]
1.5MNP	21.7	1.66	4.0	43.4
3MNP	25.1	1.89	4.4	50.2
5MNP	46.8	1.81	4.3	93.6
7MNP	65.2	1.83	4.1	130.4
10MNP	85.6	2.30	4.4	220.8

exponent  $P$  were around 4, as it is expected for this kind of structures. The dependence of  $D_f$  and  $R_g$  as a function of the nanoparticle content is consistent with the formation of larger clusters with a more compact architecture. In addition, the evolution of  $D_f$  values indicate that for those samples with nanoparticles content between 1.5 and 7 wt.%, the clusters tend to have a two-dimensional architecture,<sup>[47]</sup> while for the most concentrated sample (10MNP), the magnetic nanoparticles are arranged to form a three-dimensional structure.

The aggregate size  $\xi$  (related with SCs in STEM section) is reflected in the parameter  $R_g$ . Then, taking into account the obtained  $D_f$  values, we can assume that the shape of the SCs is closer to a disk of radius  $R$  for samples loaded with 1.5, 3, 5, and 7 wt.%, while for the sample loaded with 10 wt.% it is possible to consider a spherical shape for the small clusters. Under this consideration, the size of the clusters with a two dimensional architecture can be obtained by  $\xi = 2R_g$ ,<sup>[48]</sup> while for sample 10MNP the cluster size can be achieved by means  $2(5/3)^{1/2} R_g$ .<sup>[49]</sup> These values are shown in **Table 1** and correlate satisfactorily with the sizes of the SCs observed by STEM.

### 3.3. Magnetic Characterization

The magnetic properties, such as coercive field ( $H_c$ ), temperature at which there is a maximum in the ZFC curve ( $T_{max}$ ), irreversibility temperature ( $T_i$ ), and saturation magnetization ( $M_s$ ) were determined by means of the magnetization thermal dependence (ZFC-FC) and the field dependence of magnetization with temperature. The obtained results indicate that as the nanoparticle content increases, the strength of the dipolar interactions among the particles also increases. This is evidenced by the shift of the  $T_{max}$  (**Figure 5** and **Table 2**), from 100 to 185 K when the MNP concentration varied from 1.5 to 10 wt.%. Additionally, the width of the blocking temperature distribution (determined from the derivative  $d(\text{ZFC-FC})/dT$ ) becomes larger as the nanoparticle content increases.<sup>[44]</sup> Other effects, for example, higher polydispersity or larger magnetic

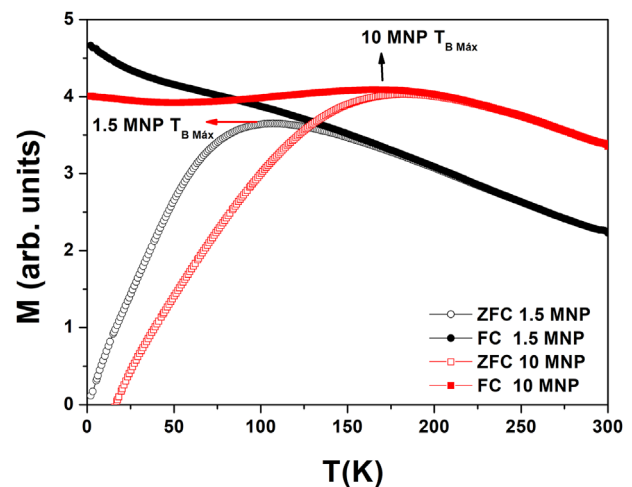


**Figure 5.** Magnetization versus temperature (ZFC-FC) for the samples with 1.5 and 10 wt.% of MNP.

**Table 2.**  $T_{\max}$  and  $T_i$  (both obtained from ZFC-FC curves) and magnetization at high field ( $M_s$ ) and coercive field ( $H_c$ ) (both obtained from  $M$  vs.  $H$  curves at different temperatures) as functions of the MNP concentration.

Sample	$T_{\max}$ [K]	$T_i$ [K]	$M_s$ [ $\text{emu g}^{-1}$ ] ( $H = 20 \text{ kOe}$ ), 2 K	$H_c$ [Oe] 2 K	$M_s$ [ $\text{emu g}^{-1}$ ] ( $H = 20 \text{ kOe}$ ), 300 K
1.5MNP	100	122	0.69	238	0.29
3MNP	123	157	1.89	243	1.14
5MNP	144	150	2.75	271	2.20
7MNP	167	179	3.22	302	2.53
10MNP	185	198	5.20	346	4.26

nanoparticle sizes, could also lead to an increase of  $T_{\max}$ . These effects are usually explained based on the variation in the polydispersity and/or larger nanoparticle sizes. Since all the composites have been prepared using the same bio-based polymer matrix and the same batch of magnetic nanoparticles, the concentration of MNP becomes the sole factor responsible for the increase of dipolar interactions.<sup>[50]</sup>

The increase of dipolar interactions as the nanoparticle concentration increases is a consequence of the related reduction of the interparticle distance. The presence of magnetic nanoparticles agglomeration or strengthening of the dipolar interactions can also be corroborated with the increase in  $T_i$  (defined as the threshold temperature above which FC and ZFC curves coincide). At this temperature, all the particles (even those forming agglomerated clusters) are in an unblocked magnetic state and they behave as superparamagnetic. According to our results, in all the nanocomposites, the  $T_i$  was found below 200 K, indicating a superparamagnetic behavior above this temperature. The small difference between  $T_{\max}$  and  $T_i$  indicates a narrow size distribution of the particles.

In addition, from the low temperature dependence of FC curve (below  $T_{\max}$ ) can be confirmed that dipolar interactions in the 10 wt.% MNP sample are stronger in comparison to those samples with lower content of magnetic nanoparticles. This sample presents a quasi-plateau of low temperature saturation in FC curves while the magnetization increases with decreasing temperature for the material with 1.5 wt.% of MNPs (Figure 5).

Magnetization as a function of the applied field was measured at different temperatures (2, 15, 100, and 300 K), for all the investigated nanocomposites (see Figure S5, Supporting Information). **Figure 6** shows field-dependent magnetization for samples loaded with 1.5 and 10 wt.% MNP at 300 K. Detail of the central area of the magnetization loops is shown in the inset of this figure. The superparamagnetic behavior at room temperature can be corroborated by the absence of hysteresis in the magnetization loop (inset of Figure 6). At temperatures below  $T_i$ , the magnetic particles are blocked, and consequently, hysteresis appears in the magnetization measurements, which is reflected in not null coercive fields (Table 2 and Table S1, Supporting Information).

### 3.4. Glass Transition Temperature and its Relationship with the Materials Shape Recovery

To analyze and to take advantage of the potential shape recovery response of these materials, a preliminary analysis of their dynamic-mechanical properties was performed. The

information obtained for the glass transition temperatures was considered for the selection of the switching temperature of these functional nanocomposites. The characteristics of the  $\tan \delta$  peak of the unfilled polymer and nanocomposites containing 1 and 9 wt.% of MNPs were discussed in a previous publication and they were confirmed for this work completing the whole series of nanocomposites.<sup>[39]</sup> The unfilled matrix presented a maximum in the damping factor at 20 °C, while all the nanocomposites presented also a second peak at higher temperatures in the range of 44–50 °C.<sup>[39]</sup> A figure of  $\tan \delta$  for polymer and composites is provided as Figure S6, Supporting Information.

The matrix chosen to prepare the composites presents shape memory behavior (a complete characterization of this material was reported in previous works)<sup>[39,40,51]</sup> and the addition of the nanoparticles did not suppress this property.<sup>[39]</sup>

### 3.5. Magnetic Nanoparticle Heating

The activation of the shape recovery in shape memory polymers is usually achieved by direct contact of the sample with a thermal bath or by using an external heat source. Both strategies result in serious limitations on the application of these materials. The use of magnetic nanoparticles and an alternating magnetic field appears as an alternative method that allows the remote

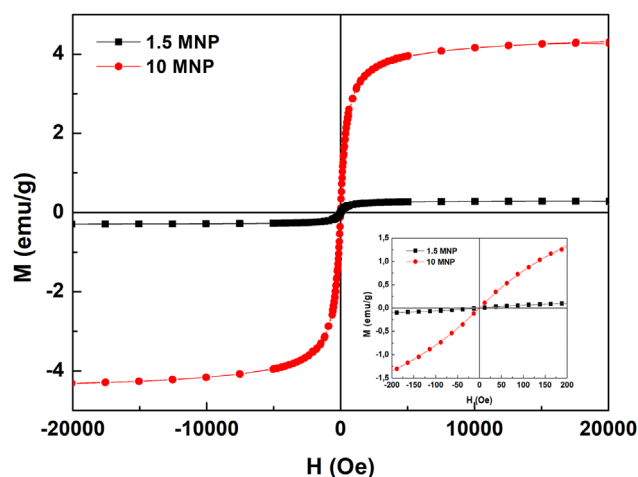


**Figure 6.** Magnetization versus applied field for the nanocomposites with 1.5 and 10 wt.% of MNP at 300 K. Right corner inset: magnifications of the central area of the magnetization loops.

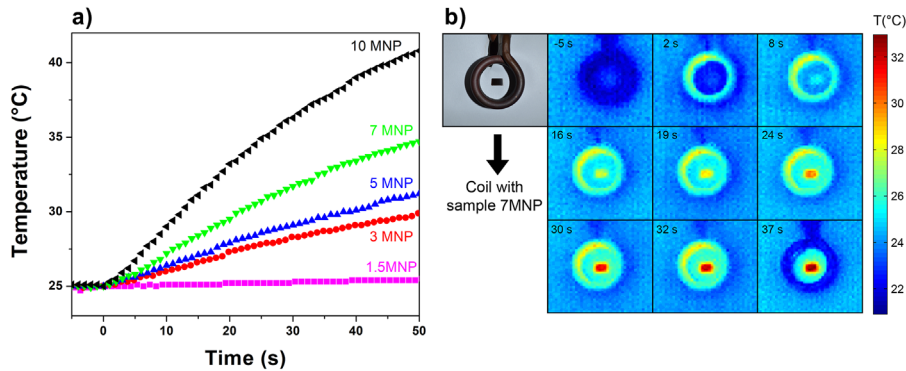


**Figure 7.** a) First 50 s of the magnetothermal measurements for nanocomposites with different content of MNP under application of an alternating magnetic field turned on at 0 s. b) Series of images taken with a thermographic camera at different times (the field was turned on at 0 s and turned off at 36 s).

activation. To achieve this objective, it is necessary to obtain magnetic nanoparticles with high enough SAR. Particles with high SAR values allow the obtention of samples capable to reach the temperature necessary to activate the shape recovery process by using a MNP concentration in the matrix that is also low enough to avoid a detrimental effect on this desirable property.

SAR was determined by means of magneto-calorimetric measurements in magnetic nanoparticle heating experiments: the sample is exposed to an alternating magnetic field while its temperature is registered and then SAR was calculated from these measurements. **Figure 7a** shows the heating curves for samples with different content of MNPs under the influence of a magnetic field with amplitude of  $48 \text{ kA m}^{-1}$  and frequency of 260 kHz. As can be expected, the temperature rises faster and reaches higher values as the amount of MNPs increases. The time required to reach a temperature of  $30^\circ\text{C}$  (starting from room temperature of  $25^\circ\text{C}$ ) was 33 s for 3MNP, 21 s for 5MNP, 10 s for 7MNP, and 6 s for 10MNP.

Figure 7b shows the images taken with a thermographic camera (TESTO 870-1) at different times after turning on an alternating field of 260 kHz and  $54 \text{ kA m}^{-1}$  for the sample 7MNP. The first and last images correspond to images without applied field, where the blue color is related to the lower temperatures. The sequence clearly shows the gradual and desired homogenous heating of the sample. The homogeneous

distribution inside the sample, of the MNPs that act as nanoheaters, ensures the homogenous increase of temperature, resulting in another good property of the material considered.

The SAR values were determined from the derivative of temperature with time ( $dT/dt$ ) evaluated at the temperature at which the medium without MNP (unfilled matrix) reaches the thermal equilibrium under the same experimental conditions used with the nanocomposites ( $T_{\text{equilibrium}} = 29.5^\circ\text{C}$ ), thus the SAR values were calculated as

$$\text{SAR} = \frac{dT}{dt} \frac{c}{m_{\text{MNP}}} \quad (2)$$

where  $T$  is temperature,  $t$  is time,  $c$  is the specific heat capacity ( $\text{J g}^{-1} \text{K}^{-1}$ ) of the sample and  $m_{\text{MNP}}$  is the nanoparticle weight fraction. The specific heat capacity ( $c$ ) of the samples was obtained from differential scanning calorimetry (DSC) runs (not shown) following a standard procedure (ASTM 1269-01). It was found that this property ( $c$ ) was independent of the MNP concentration for temperatures lower than  $70^\circ\text{C}$ . Assuming a linear function for  $c$  versus  $T$ , a good fitting was obtained and the value of  $c$  determined at  $T = 29.5 \pm 7^\circ\text{C}$  was  $c = 1.63 \pm 0.6 \text{ J g}^{-1} \text{K}^{-1}$ .

**Figure 8a** and **b** present  $dT/dt$  and SAR parameter as a function of the MNP content, respectively. It can be noticed that

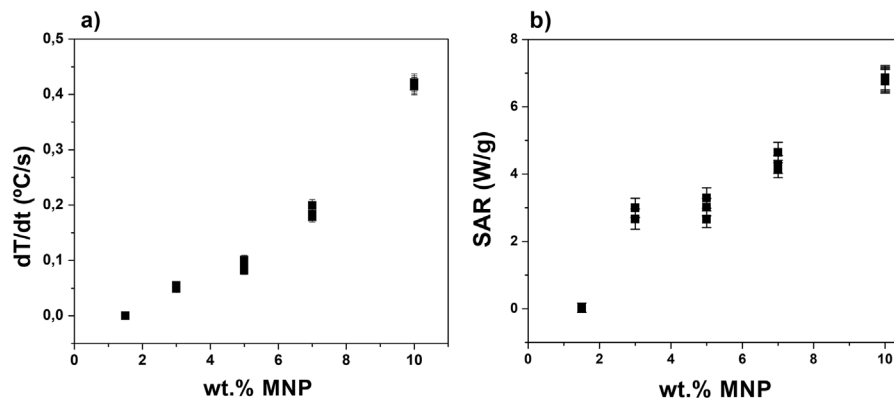


**Figure 8.** a)  $dT/dt$  and b) SAR as a function of the MNP content in the copolymer.



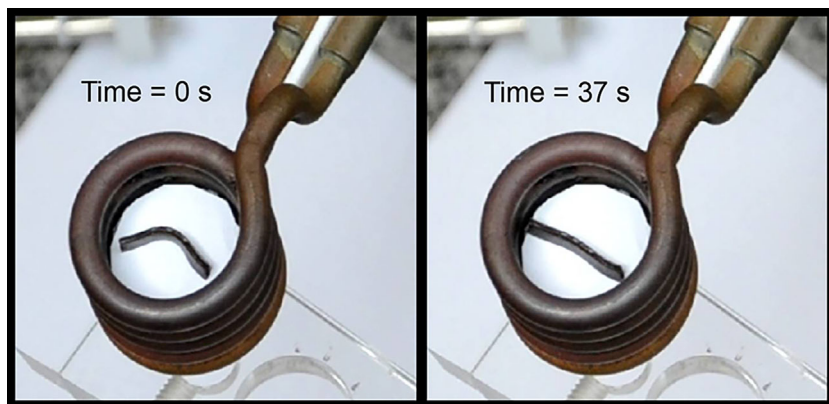


**Figure 9.** Shape recovery process of the nanocomposite 10MNP in a magnetic field.

both properties increase with the concentration of MNP into the matrices. For non-interacting particles, the SAR is independent of concentration. The change of SAR with MNP content is related to a vary in the relaxation time of the MNP's response to the alternating magnetic field. The increasing MNP concentrations (i.e., shorter interparticle mean distances) result in greater dipolar interactions between the MNPs, which modify the magnetic relaxation time of the particles in the composites. This analysis agrees with the discussion of the FC/ZFC and microscopy results that clearly show agglomeration and interaction among particles.

### 3.6. Magnetic Remote Activation of Shape Recovery

To test the possibility of activating the shape recovery of the nanocomposites using a magnetic field as the source of heating, the following experiment was performed: the deformed specimen (exhibiting a temporary fixed shape) was placed in the center of a coil and the changes experienced by the sample were video-recorded while the alternating magnetic field was applied. When the temperature of the sample reached a value higher than the  $T_g$  of the material, the recovery of the original shape took place.<sup>[52]</sup> This effect can be observed in **Figure 9** for the composite with 10MNP. Both, the heating rate and consequently, the time necessary to recover the original shape depend on the amount of MNP in the material.

This experiment confirms that magnetic remote activation properties have been successfully achieved in a partially “green” polymeric matrix with shape memory behavior. Achievement of this goal confirms that the nanocomposites based on vegetable oil and magnetic iron oxides nanoparticles (MNPs) presented in this work are valuable materials of interest in potential applications such as in sensors and actuators.

## 4. Conclusions

Remote shape recovery was successfully activated in biobased magnetic nanocomposites. The unfilled thermoset matrix based in raw tung oil and styrene presented shape memory properties

with a switching temperature determined by its glass transition temperature. In this work, it was demonstrated that the nanocomposites benefitted from this characteristic of the polymeric matrix, but also presented synergic effects. The dispersion of the nanoparticles in the polymer lead to different morphologies depending on the concentration, and for MNPs content higher than 1.5 wt.%, a bi-modal curve of cluster size distribution was observed. The sizes of the small fractal clusters for the sample with 10 wt.% MNP were in the order of 220.8–314 nm as determined from SAXS and STEM, respectively. The results showed that all the nanocomposites prepared in the conditions of the work, presented superparamagnetic behavior at room temperature and the results clearly denoted that the

agglomeration increases with MNP content leading to stronger dipolar interactions. Lastly, it was possible to heat all the materials investigated by remotely applying an alternating magnetic field. The temperatures reached were directly related to the concentration of magnetic iron oxides. The shape recovery process was activated by this means and the permanent original shape was recovered. The sample with 10 wt.% MNP presented the best heating behavior with the shortest time for shape recovery.

## Supporting Information

Supporting Information is available from the Wiley Online Library or from the author.

## Acknowledgments

Oscar Moscoso Londoño and Marcelo Knobel acknowledge FAPESP (2014/26672-8) and CNPq (Brazilian agencies). The work at UNICAMP of Cintia Meiorin was supported by CNPq (506394/2013-1), Brazil and CONICET in Argentina. Small-angle X-ray scattering data were acquired at beamline D11A-SAXS1 (17036), D11A-SAXS2 (14355) at LNLS (Campinas, SP, Brazil) and STEM images (17596) were taken by Fabiano E. Montoro (fabiano.montoro@lnnano.cnpem.br) at the LNNano of National Nanotechnology Laboratory (CNPEM, Campinas, Brazil). The Argentinian authors thank Cooperativa Agrícola de Picada Libertad for the supply of tung oil and the financial support of CONICET (PIP 112 201101 00866 and PIP 112 201101 00720), UNMdP (15/G430-ING 436/15), and ANPCyT (PICT 2013-1535) from Argentina.

## Conflict of Interest

The authors declare no conflict of interest.

## Keywords

functional nanocomposites, magnetic nanoparticle heating, magnetic properties, remote activation of shape recovery, vegetable oil based polymers

Received: April 18, 2018  
Revised: October 8, 2018  
Published online: November 13, 2018

- [1] H. Baumann, M. Bühler, H. Fochern, F. Hirsinger, H. Zobelein, J. Falbe, *Angew. Chem. Int. Ed. English* **1988**, 27, 41.
- [2] U. Biermann, W. Friedt, S. Lang, W. Lühs, G. Machmüller, J. O. Metzger, M. Rüschen Klaas, H. J. Schäfer, M. P. Schneider, *Angew. Chem. Int. Ed. Engl.* **2000**, 39, 2206.
- [3] K. Hill, *Pure Appl. Chem.* **2000**, 72, 1255.
- [4] P. L. Nayak, *J. Macromol. Sci. Part C Polym. Rev.* **2000**, 40, 1.
- [5] J. O. Metzger, *Chemosphere* **2001**, 43, 83.
- [6] S. Warwel, F. Brüse, C. Demes, M. Kunz, M. Rüschen Klaas, *Chemosphere* **2001**, 43, 39.
- [7] H. N. Rabetafika, M. Paquot, P. Dubois, *Biotechnol. Agron. Soc. Environ.* **2006**, 10, 185.
- [8] K. F. Adekunle, *Open J. Polym. Chem.* **2015**, 5, 34.
- [9] S. N. Khot, J. J. Lascala, E. Can, S. S. Morye, G. I. Williams, G. R. Palmese, S. H. Kusefoglu, R. P. Wool, *J. Appl. Polym. Sci.* **2001**, 82, 703.
- [10] J. J. La Scala, J. M. Sands, J. A. Orlicki, E. J. Robinette, G. R. Palmese, *Polymer* **2004**, 45, 7729.
- [11] Y. Xia, R. C. Larock, *Green Chem.* **2010**, 12, 1893.
- [12] M. A. Mosiewicki, M. I. Aranguren, J. Borrajo, *J. Appl. Polym. Sci.* **2005**, 97, 825.
- [13] M. W. Formo, E. Jungermann, F. A. Norris, N. O. V. Sonntag, *Bailey's Industrial Oil and Fat Production*, 4th ed., vol. 1 (Ed: D. Swern), Wiley, New York, New York **1985**.
- [14] R. G. Kinabrew, *Tung Oil in Mississippi; the Competitive Position in the Industry*. Univ. Mississippi, Oxford, MS **1952**.
- [15] A. M. Fernandez, A. Conde, *Polymer Applications of Renewable-Resource Materials*. Springer US, Boston, MA **1983**, pp. 289–302.
- [16] Y. Lu, L. Tighzert, P. Doble, D. Erre, *Polymer* **2005**, 46, 9863.
- [17] A. Lendlein, R. Langer, *Science* **2002**, 296, 1673.
- [18] Y. Liu, H. Du, L. Liu, J. Leng, *J. Smart Mater. Struct.* **2014**, 23, 23001.
- [19] X. Luo, P. T. Mather, *ACS Macro Lett.* **2013**, 2, 152.
- [20] M. D. Hager, S. Bode, C. Weber, U. S. Schubert, *Prog. Polym. Sci.* **2015**, 49–50, 3.
- [21] Q. Zhao, H. J. Qi, T. Xie, *Prog. Polym. Sci.* **2015**, 49–50, 79.
- [22] J. Hu, S. Chen, *J. Mater. Chem.* **2010**, 20, 3346.
- [23] A. Avendano-Bolivar, T. Ware, D. Arreaga-Salas, D. Simon, W. Voit, *Adv. Mater.* **2013**, 25, 3095.
- [24] W. Wang, J. Salazar, H. Vahabi, A. Joshi-Imre, W. E. Voit, A. K. Kota, *Adv. Mater.* **2017**, 29, 1700295.
- [25] M. L. Auad, T. Richardson, M. Hicks, M. A. Mosiewicki, M. I. Aranguren, N. E. Marcovich, *Polym. Int.* **2012**, 61, 321.
- [26] T. B. Richardson, M. A. Mosiewicki, C. Uzunpinar, N. E. Marcovich, M. I. Aranguren, F. Kilinc-Balci, R. M. Broughton, M. L. Auad, *Polym. Compos.* **2011**, 32, 455.
- [27] M. L. Auad, M. A. Mosiewicki, T. Richardson, M. I. Aranguren, N. E. Marcovich, *J. Appl. Polym. Sci.* **2010**, 115, 1215.
- [28] K. Gall, M. L. Dunn, Y. Liu, D. Finch, M. Lake, N. A. Munshi, *Acta Mater.* **2002**, 50, 5115.
- [29] R. E. Rosensweig, *J. Magn. Magn. Mater.* **2002**, 252, 370.
- [30] D. F. Coral, P. Mendoza Zélis, M. E. de Sousa, D. Muraca, V. Lassalle, P. Nicolás, M. L. Ferreira, M. B. Fernández van Raap, *J. Appl. Phys.* **2014**, 115, 043907.
- [31] D. F. Coral, P. Mendoza Zélis, M. Marciello, M. del Puerto Morales, A. Craievich, F. H. Sánchez, M. B. Fernández van Raap, *Langmuir* **2016**, 32, 1201.
- [32] M. Y. Razzaq, M. Anhalt, L. Frommann, B. Weidenfeller, *Mater. Sci. Eng. A* **2007**, 471, 57.
- [33] B. Weidenfeller, M. J. Anhalt, *Thermoplast. Compos. Mater.* **2014**, 27, 895.
- [34] A. M. Schmidt, *Macromol. Rapid Commun.* **2006**, 27, 1168.
- [35] R. Mohr, K. Kratz, T. Weigel, M. Lucka-Gabor, M. Moneke, A. Lendlein, *Proc. Natl. Acad. Sci.* **2006**, 103, 3540.
- [36] D. Yang, W. Huang, X. He, M. Xie, *Polym. Int.* **2012**, 61, 38.
- [37] C. M. Yakacki, R. Shandas, C. Lanning, B. Rech, A. Eckstein, K. Gall, *Biomaterials* **2007**, 28, 2255.
- [38] J. Puig, C. E. Hoppe, L. A. Fasce, C. J. Pérez, Y. Piñero-Redondo, M. Bañobre-López, M. A. López-Quintela, J. Rivas, R. J. Williams, *J. Phys. Chem. C* **2012**, 116, 13421.
- [39] C. Meiorin, D. Muraca, K. R. Pirota, M. I. Aranguren, M. A. Mosiewicki, *Eur. Polym. J.* **2014**, 53, 90.
- [40] C. Meiorin, M. I. Aranguren, M. A. Mosiewicki, *J. Appl. Polym. Sci.* **2012**, 124, 5071.
- [41] J. Kohlbrecher, A program for fitting simple structural models to small angle scattering data, Paul Scherrer Institute Laboratory for Neutron Scattering Villigen, Switzerland, **2014**.
- [42] C. Meiorin, O. M. Londoño, D. Muraca, L. M. Socolovsky, K. R. Pirota, M. I. Aranguren, M. Knobel, M. A. Mosiewicki, *Mater. Chem. Phys.* **2016**, 175, 81.
- [43] A. V. Teixeira, I. Morfin, F. Ehrburger-Dolle, C. Rochas, P. Panine, P. Licinio, E. Geissler, *Compos. Sci. Technol.* **2003**, 63, 1105.
- [44] O. Moscoso-Londoño, J. S. Gonzalez, D. Muraca, C. E. Hoppe, V. A. Alvarez, A. López-Quintela, L. M. Socolovsky, K. R. Pirota, *Eur. Polym. J.* **2013**, 49, 279.
- [45] O. Moscoso-Londoño, P. Tancredi, D. Muraca, P. Mendoza Zélis, D. Coral, M. B. Fernández van Raap, U. Wolff, V. Neu, C. Damm, C. L. P. de Oliveira, K. R. Pirota, M. Knobel, L. M. Socolovsky, *J. Magn. Magn. Mater.* **2017**, 428, 105.
- [46] G. Beaucage, *J. Appl. Crystallogr.* **1995**, 28, 717.
- [47] J. M. Orozco-Henao, D. F. Coral, D. Muraca, O. Moscoso-Londoño, P. Mendoza Zélis, M. B. Fernandez van Raap, S. K. Sharma, K. R. Pirota, M. Knobel, *J. Phys. Chem. C* **2016**, 120, 12796.
- [48] R. J. Roe, *Methods of X-Ray and Neutron Scattering in Polymer Science*. Oxford University Press, New York, NY **2000**.
- [49] L. A. Feigin, D. I. Svergun, *Structure Analysis by Small-Angle X-Ray and Neutron Scattering*. Plenum Press/Springer, New York **1987**.
- [50] A. Demortière, P. Panissod, B. P. Pichon, G. Pourroy, D. Guillon, B. Donnio, S. Bégin-Colin, *Nanoscale* **2011**, 3, 225.
- [51] C. Meiorin, M. I. Aranguren, M. A. Mosiewicki, *Polym. Int.* **2012**, 61, 735.
- [52] X. Zheng, S. Zhou, Y. Xiao, X. Yu, X. Li, P. Wu, *Colloids Surf. B Biointerfaces* **2009**, 71, 67.